



# Spatial Expansion and Speeds of Type III Electron Beam Sources in the Solar Corona

Hamish A. S. Reid  and Eduard P. Kontar 

SUPA School of Physics and Astronomy, University of Glasgow, Glasgow G12 8QQ, UK; [hamish.reid@glasgow.ac.uk](mailto:hamish.reid@glasgow.ac.uk)  
Received 2018 July 6; revised 2018 September 4; accepted 2018 September 30; published 2018 November 12

## Abstract

A component of space weather, electron beams are routinely accelerated in the solar atmosphere and propagate through interplanetary space. Electron beams interact with Langmuir waves resulting in type III radio bursts. They expand along the trajectory and, using kinetic simulations, we explore the expansion as the electrons propagate away from the Sun. Specifically, we investigate the front, peak, and back of the electron beam in space from derived radio brightness temperatures of fundamental type III emission. The front of the electron beam travels at speeds from  $0.2c$  to  $0.7c$ , significantly faster than the back of the beam, which travels at speeds between  $0.12c$  and  $0.35c$ . The difference in speed between the front and the back elongates the electron beam in time. The rate of beam elongation has a 0.98 correlation coefficient with the peak velocity, in line with predictions from type III observations. The inferred speeds of electron beams initially increase close to the acceleration region and then decrease through the solar corona. Larger starting densities and harder initial spectral indices result in longer and faster type III sources. Faster electron beams have higher beam energy densities, and produce type IIIIs with higher peak brightness temperatures and shorter FWHM durations. Higher background plasma temperatures also increase speed, particularly at the back of the beam. We show how our predictions of electron beam evolution influences type III bandwidth and drift rates. Our radial predictions of electron beam speed and expansion can be tested by the upcoming in situ electron beam measurements made by *Solar Orbiter* and *Parker Solar Probe*.

**Key words:** solar wind – Sun: corona – Sun: flares – Sun: particle emission – Sun: radio radiation

## 1. Introduction

Solar electron beams, accelerated via magnetic instabilities in the solar atmosphere, do not simply propagate scatter-free through the solar corona and interplanetary space. They interact with the background plasma, which results in them not propagating at a constant velocity. One such resonant interaction is the excitation of Langmuir waves through the bump-in-tail instability (Ginzburg & Zhelezniakov 1958). Electron beams and Langmuir waves are detected in situ together (Gurnett & Frank 1975; Gurnett & Anderson 1976), along with type III radio bursts which are generated via wave-wave interactions by the Langmuir waves. Remote sensing type III bursts at high frequencies provide information about electron beam speeds in the solar atmosphere where in situ measurements are not currently possible. The energy exchange between the electron beam and Langmuir waves modifies the electron distribution (e.g., Zaitsev et al. 1972; Magelssen & Smith 1977; Mel’Nik & Kontar 1998; Kontar 2001a).

To estimate electron beam velocities via remote sensing, the frequency drift rate  $ft$  of type III bursts is often used, where  $f$  is the frequency. Because the plasma frequency decreases as a function of distance from the Sun, the frequency drift rate provides information about how fast the electron beam travels through the heliosphere. Type III drift rates decrease in magnitude as a function of decreasing frequency. This is typically related to the decreasing magnitude of the background electron density gradient at farther distances from the Sun (Kontar 2001b; Ratcliffe et al. 2012). A power-law dependence over four orders of magnitude was found by Alvarez & Haddock (1973) combining results from numerous studies.

Drift rates have been reported to be slightly lower at higher frequencies (e.g., Achong & Barrow 1975; Mel’Nik et al. 2011). They are usually found using the evolution of the peak flux in time although the onset time is occasionally used. Type III drift rates using the onset time have been shown to be faster than when the peak time is used, which in turn are faster than when the decay time is used (Reid & Kontar 2018). Type III drift rates are also influenced by the radio emission mechanism that converts Langmuir waves to radio waves and the subsequent radio wave propagation from source to observer (e.g., Kontar et al. 2017). However, in this work we concentrate on how the beam dynamics influences the type III drift rate.

Velocities of electron beams deduced from type III bursts are measured in fractions of the speed of light. Typical velocities are between 0.2 and  $0.5c$  (e.g., Wild et al. 1959; Alvarez & Haddock 1973; Suzuki & Dulk 1985; Reid & Ratcliffe 2014) although relativistic velocities ( $>0.6c$ ) have been found in the corona (Poquerusse 1994; Klassen et al. 2003). A recent study by Reid & Kontar (2018) of 31 type III bursts estimated velocities deduced from the rise, peak, and decay times of type III bursts to be  $0.2c$ ,  $0.17c$ , and  $0.15c$  respectively. Exciter speeds were found to be significantly lower in the interplanetary medium from type III bursts below 20 MHz (Fainberg et al. 1972; Dulk et al. 1987; Krupar et al. 2015; Reiner & MacDowall 2015), going down to  $0.1c$  or below. Electron beams were found to decelerate on their way to the Sun; a constant velocity was not a good approximation. Typical deceleration values below 20 MHz have been found around  $10 \text{ km s}^{-2}$  (Krupar et al. 2015).

While a single exciter velocity is typically attributed to electron beams from type III bursts, the Langmuir wave-generating beams have a broad distribution in energy space (e.g., Zaitsev et al. 1972). The electron beam and the resonating Langmuir waves can be described as a beam-plasma structure using gas-dynamic theory (e.g., Ryutov & Sagdeev 1970;



Original content from this work may be used under the terms of the [Creative Commons Attribution 3.0 licence](https://creativecommons.org/licenses/by/3.0/). Any further distribution of this work must maintain attribution to the author(s) and the title of the work, journal citation and DOI.

Mel'Nik 1995; Kontar' et al. 1998; Mel'Nik et al. 1999; Kontar & Mel'Nik 2003). The electron and Langmuir waves travel together through a constant exchange of energy, the electron distribution relaxing to a plateau in velocity space between  $v_{\min}$  and  $v_{\max}$ . It was shown that the resulting beam–plasma structure (Mel'Nik et al. 1999; Kontar & Mel'Nik 2003) moves through space with the average velocity of the electrons  $v_{\text{bps}} = (v_{\max} + v_{\min})/2$ , where  $v_{\max}$  is the speed of the electrons at injection and  $v_{\min}$  is the minimum electron speed. Electron beams injected at the Sun are not necessarily Maxwellian, but the collective behavior exhibited by the beam–plasma structure helps explain why near-constant beam velocities are inferred from type III bursts (e.g., Mel'Nik et al. 1999; Kontar & Mel'Nik 2003).

Simulations of electron beams propagating through the solar corona and interplanetary space, interacting with Langmuir waves, have been carried out for decades (e.g., Takakura & Shibahashi 1976; Magelssen & Smith 1977). For simulations over significant distances, the quasilinear description (e.g., Vedenov 1963) is typically used. From observations of electrons in situ at 1 au (Lin et al. 1981; Krucker et al. 2007) and from estimations from X-ray observations (Holman et al. 2011), a power-law electron beam is commonly assumed as the injection function. Previous numerical studies (e.g., Reid & Kontar 2013; Li & Cairns 2014; Ratcliffe et al. 2014) have shown that, over large distances of a few solar radii or more, the velocity range of electrons that generates the bulk of the Langmuir waves decreases. This is consistent with the decrease in type III drift rate as a function of frequency (Fainberg et al. 1972; Krupar et al. 2015).

If electrons propagated freely, the beam length would increase through velocity dispersion as a beam consists of electrons with a range of velocities. As faster electrons outpace slower ones, the fastest electrons will travel a distance of  $v_{\max}\Delta t$  while the slowest will travel a distance of  $v_{\min}\Delta t$ . The electron beam length will increase over time by  $(v_{\max} - v_{\min})\Delta t$  over some time  $\Delta t$ . However, it appears that free electron propagation is an oversimplification, and electron velocities will change during propagation through wave-particle interactions and/or pitch-angle scattering. How electron beam length thus develops as a function of time is poorly understood.

The type III parameter most associated with the electron beam length is the instantaneous bandwidth: the width in frequency between the minimum and maximum frequency at any point in time. The type III bandwidth provides information about where the electron beam is able to radiate at any given time; this has not been extensively studied in the past. Hughes & Harkness (1963) defined the bandwidth from the leading edge to the highest frequency, finding a bandwidth of 100 MHz from a leading edge of 100 MHz. Mel'Nik et al. (2011) defined the instantaneous bandwidth as the half-power bandwidth, finding a value of 15 MHz around 18 MHz for powerful type III bursts. To account for asymmetric bandwidth profiles, Reid & Kontar (2018) defined the bandwidth using the rise and decay times of the type III emission to estimate  $f_{\min}$  and  $f_{\max}$  for each point in time. The instantaneous bandwidth  $\Delta f = f_{\max} - f_{\min}$  at the frequency with roughly peak intensity. Bandwidths of 20 MHz were found around 50 MHz. Both Mel'Nik et al. (2011) and Reid & Kontar (2018) found the bandwidth to vary roughly as  $\Delta f = 0.6f$ .

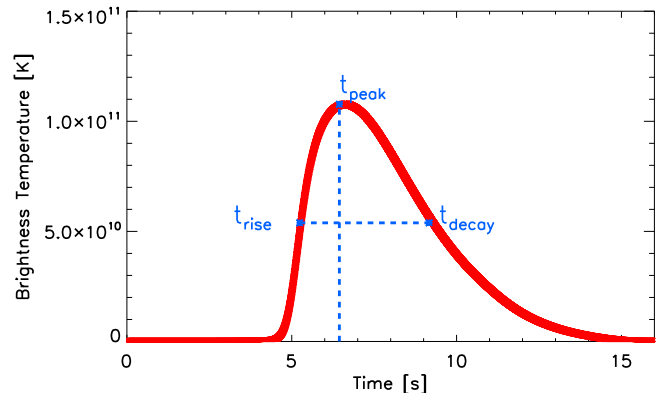


**Figure 1.** Time profile of the radio brightness temperature deduced from the Langmuir waves at 30 MHz or  $0.76 R_{\odot}$ . The rise, peak, and decay times corresponding to the peak value and half-width half-maximum are indicated.

In this study we investigate both the velocity of electron beams and their length as they travel through the solar corona. We start by defining different regions of the electron beam: the front, peak, and back. We then show in Section 3 how these parameters evolve with time and what causes their evolution. How the change in the initial beam parameters affects the beam velocity and length is shown in Section 4, along with the effect of the background plasma electron temperature. We explore the effects on type III properties from injecting electron beams with different parameters in Section 5. The results are discussed in Section 6, with conclusions provided in Section 7.

## 2. Simulation Model

### 2.1. Kinetic Model

To investigate the length and velocity of an electron beam we used a 1D self-consistent kinetic model (Kontar 2001c) of the electron distribution function  $f(v, r, t)$  (electrons  $\text{cm}^{-3} \text{s}^{-1}$ ) and the spectral energy of Langmuir waves  $W(v, r, t)$  ( $\text{erg cm}^{-2}$ ). The model calculated the 1D propagation of the electrons along the direction of the guiding magnetic field in the WKB approximation, where waves are treated as quasi-particles interacting resonantly ( $\omega_{pe} = kv$ , where  $\omega_{pe}$  is the plasma frequency) with the electrons.

An in-depth description of the kinetic equations, source model, and background plasma model can be found in Reid & Kontar (2017). The same background plasma density model, obtained using the equations for a stationary spherical symmetric solution (Parker 1958) with a normalization factor by Mann et al. (1999), is used in all simulations. No density fluctuations are added. The source function parameters do vary between simulations. The source function is given by

$$S(v, r, t) = A_v v^{-\alpha} \exp\left(-\frac{r^2}{d^2}\right) A_t \exp\left(-\frac{(t - t_{\text{inj}})^2}{\tau^2}\right), \quad (1)$$

where  $A_v = n_b(\alpha - 1)/(v_{\min}^{1-\alpha} - v_{\max}^{1-\alpha})$  is a normalization constant that sets the beam density  $n_b$  [ $\text{cm}^{-3}$ ]. The constant  $A_t = (\tau\sqrt{\pi})^{-1}$  normalizes the integral of the exponential involving time to one. The characteristic variables that define the behavior of the source function in velocity, distance, and time are  $\alpha$ ,  $d$  (cm), and  $\tau$  (s), respectively.

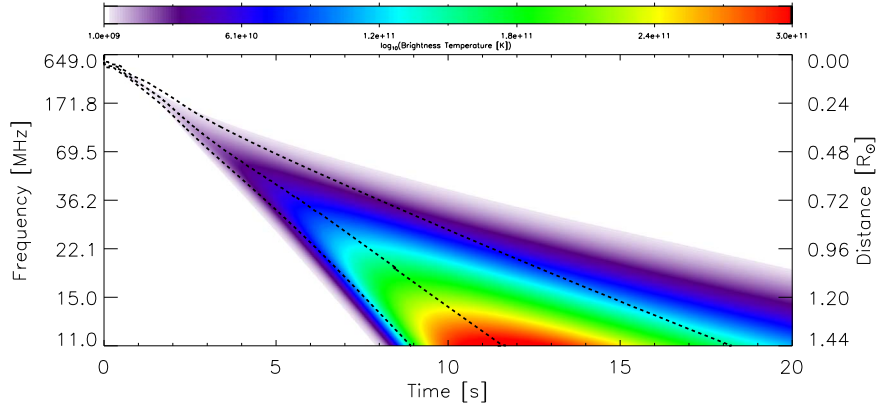


**Figure 2.** Type III brightness temperature dynamic spectrum assuming fundamental emission and a saturation of ion-sound waves, found using Equation (3) and an initial electron beam described in Table 1. The rise, peak, and decay times from the FWHM at each frequency are indicated by black dashed lines.

**Table 1**  
Initial Beam Parameters for the Electron Beam Injected into the Solar Corona

Energy Range	Velocity Range	Spectral Index	Injection Time	Beam Size	Source Height	Density Ratio
0.28–125 keV	2.6–54 $v_{\text{th}}$	$\alpha = 8.0$	$\tau = 0.001$ s	$d = 10^9$ cm	$h = 3 \times 10^9$ cm	$n_b/n_e = 0.003$

## 2.2. Radio Emission

We approximate a dynamic spectrum of fundamental emission from the Langmuir wave spectral energy density assuming a saturation level of plasma emission (Melrose 1980; Tsytovich & ter Haar 1995; Lyubchyk et al. 2017). Beam-driven Langmuir wave growth causes  $W_L \gg W_S$ , where  $W_L$  and  $W_S$  are the spectral energy density of Langmuir waves and ion-sound waves, respectively. The nonlinear decay  $L \rightarrow T + S$  causes exponential growth of ion-sound waves (e.g., Melrose 1980). This will increase both  $W_S$  and the brightness temperature  $T_T$  until such time as  $W_S \gg W_L$ . At this point the process saturates at the level

$$T_T(k, r, t) = \omega_T(r) \frac{\eta}{k_s(r)^2 k_b} \frac{W_L(k, r, t)}{\omega_L(r)} \quad (2)$$

where  $k_s$  is the wavenumber of the ion-sound waves,  $\omega_L$ ,  $\omega_T$  are the Langmuir wave and electromagnetic wave angular frequencies, and  $k_b$  is the Boltzmann constant. If we assume that  $\omega_T \approx \omega_L$  and  $k_s \approx k_L$ , then for  $\eta = (2\pi)^2$  we obtain

$$k_b T_T(k, r, t) \approx \frac{(2\pi)^2}{k_L(r)^2} W_L(k, r, t). \quad (3)$$

To obtain the brightness temperature at each position (frequency),  $T_T(r, t)$ , we use the peak value of  $T_T(k, r, t)$  for each point in space and time. The spread in  $k$  (and consequently frequency) is small for each point in space and the peak value gives very similar results to using the mean value of  $T_T(k, r, t)$  as a function of  $k$ .

## 3. Electron Beam Dynamics

When diagnosing electron beam dynamics from type III radio bursts, we are getting information about electrons that are undergoing significant wave-particle interactions with the Langmuir waves, which subsequently drive the radio emission. The bulk of the energy in the system is contained within the electrons and the Langmuir waves; the radio emission is not

energetically important. Therefore, the motion of the electron beam through the heliosphere can be modeled using the electrons and Langmuir waves alone.

In this work, we investigate the electron beam using the time profile of the fundamental radio emission estimated from the Langmuir waves (Section 2.2). For each position (frequency) we find the time,  $t_{\text{peak}}$ , at which the radio brightness temperature is highest. We then find the times which correspond to the half-width half-maximum of the intensity profile,  $t_{\text{rise}}$  and  $t_{\text{decay}}$ , of  $T_T(r, t)$ . Figure 1 shows a sample time profile of  $T_T(r, t)$  at 30 MHz ( $0.76 R_{\odot}$ ) using the simulation parameters given in Table 1, illustrating  $t_{\text{rise}}$ ,  $t_{\text{peak}}$ , and  $t_{\text{decay}}$ . For each time  $t$ , the peak of the electron beam is defined by the position where  $t \approx t_{\text{peak}}$ . Similarly, the front and back of the electron beam are at positions where  $t \approx t_{\text{rise}}$  and  $t \approx t_{\text{decay}}$ , respectively.

## 3.1. Electron Beam Properties

We initially inject an electron beam into the solar corona using the source function given in Equation (1) with parameters given in Table 1. The background temperature is set as 1 MK, giving a thermal velocity of  $v_{\text{th}} = \sqrt{k_b T_e / m_e} = 3.9 \times 10^8$  cm s $^{-1}$ . The minimum energy (velocity) is sufficiently close to the thermal distribution that the Langmuir waves are significantly damped. The maximum energy (velocity) is low enough to ignore relativistic effects (the Lorentz factor is at most 1.4), but high enough to cover the bulk of relevant energies for electrons that induce type III bursts. The spectral index is typical for accelerated electron beams, found from X-ray observations (Holman et al. 2011). The size and height are within the range of estimates found from X-ray and radio flare observations (Reid et al. 2014). The density ratio is given at the source height and corresponds to an initial background electron density of  $n_e = 3 \times 10^9$  cm $^{-3}$  (500 MHz) and an initial beam density of  $n_b = 10^7$  cm $^{-3}$ .

Figure 2 shows the dynamic spectrum of fundamental emission produced by the beam-driven Langmuir waves. The general trend of increasing intensity with decreasing frequency is shown (e.g., Dulk et al. 1998; Krupar et al. 2015; Reid &

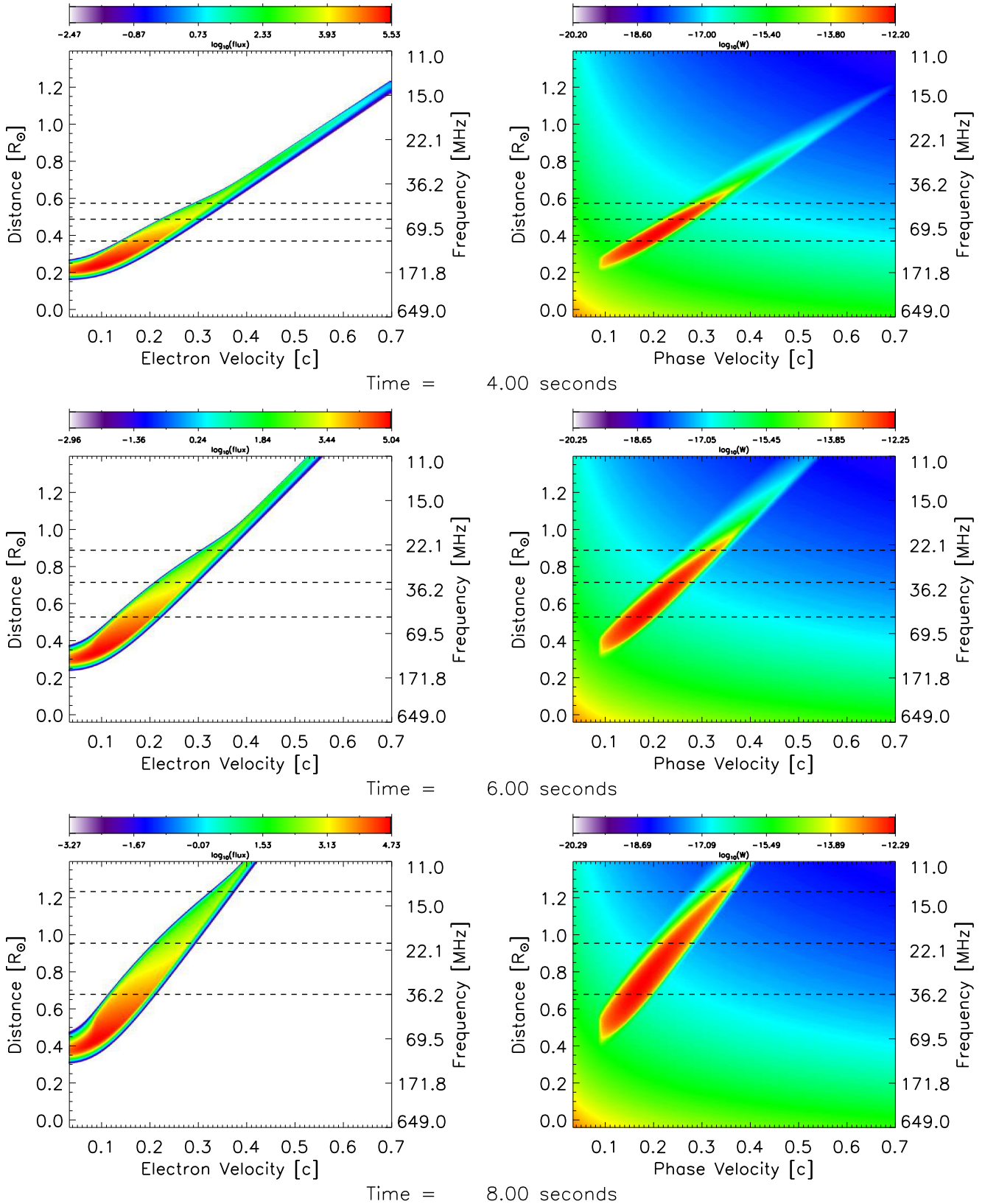


**Figure 3.** Electron flux and Langmuir wave spectral energy density at 4, 6, and 8 s after injection for the initial electron beam parameters given in Table 1. The corresponding front, peak, and back of the electron beam are shown by horizontal dashed lines, found from the derived radio brightness temperature of fundamental type III emission.

Vilmer 2017). The rise, peak, and decay times, found from the full-width half-maximum (FWHM) of the brightness temperature at each frequency are indicated.

To demonstrate how the rise, peak, and decay times of the radio emission correspond to the front, peak, and back of the electron beam, phase space snapshots of the electron

distribution function, in units of electron flux ( $\text{cm}^{-2} \text{s}^{-1} \text{eV}^{-2}$ ), and the Langmuir wave spectral energy density ( $\text{erg cm}^{-2}$ ) are shown in Figure 3. We have indicated the front, peak, and back of the beam as horizontal dashed lines.

The radio emission indicates the bulk of the electron beam in phase space, except from two parts. The first part is the very front of the electron beam. The small electron flux causes the growth rate of Langmuir waves to be insignificant compared to the background level. These electrons consequently do not diffuse in velocity space and undergo ballistic transport in our model. The second part is the back of the beam. The electron velocities are so low that Langmuir waves are strongly Landau-damped by the background plasma.

The evolution of the front, peak, and back of the electron beam, found from radio emission, are presented in Figure 4 as a function of time. We can apply a linear fit to the positions as a function of time after 3.5 s to approximate the velocities of the front, peak, and back of the electron beam. We find that the front travels faster than the peak, which in turn travels faster than the back, as one might expect. The fits are shown in Figure 4 along with the derived velocities.

We define the length of an electron beam as the distance between the front and back. The length increases as a function of time, shown in Figure 5. A linear fit to the length as a function of time gives a constant expansion velocity (increase in length as a function of time). The expansion velocity,  $\Delta v$ , is essentially the difference between the velocity at the front of the beam  $v_f$  and that at the back of the beam  $v_b$  such that  $\Delta v \approx v_f - v_b$ .

### 3.2. Electron Beam Velocity Evolution

The velocity of the front, peak, and back of the electron beam is not actually constant but changes as a function of time, shown in Figure 6. To approximate the velocity from Figure 4 we used the gradient of a straight-line fit over 30 points in space, pertaining to a distance of  $3 \times 10^9 \text{ cm}$ , with the fitting errors shown. After around 4 s, the velocity of the front and the peak of the beam increases as a function of time. This is related to a gradual increase in the velocity of the electrons that resonate with Langmuir waves, caused by physical processes including density inhomogeneity, radial expansion, and the decreasing background electron density gradient. The increase in velocity does not continue throughout the solar wind and will begin to decrease after the electron beam becomes more dilute at farther distances from the Sun. The velocity of the back of the beam decreases as a function of time. Conversely, this is related to a gradual decrease in the velocity of electrons that resonate with the Langmuir waves.

The velocity profile before 4 s is more complex, showing a sharper increase and subsequent decrease in velocity. At the earliest times the electrons that generate a substantial amount of Langmuir waves are at lower velocities. As  $t$  increases, these electrons are at higher velocities until some time  $t_p$ . At times  $t > t_p$ , the velocities of the electrons that produce substantial Langmuir waves decrease. The change in the relevant velocities of the electrons that produce the highest Langmuir wave spectral energy density is demonstrated in Figure 7. The electron flux and Langmuir wave spectral energy density as a function of velocity at different times are shown, where  $t_p \approx 3.2 \text{ s}$ . The positions,  $r$ , of  $f(v, r, t)$ , and  $W(v, r, t)$  correspond to where the spectral energy density is at a maximum (peak of the electron beam). For the different times

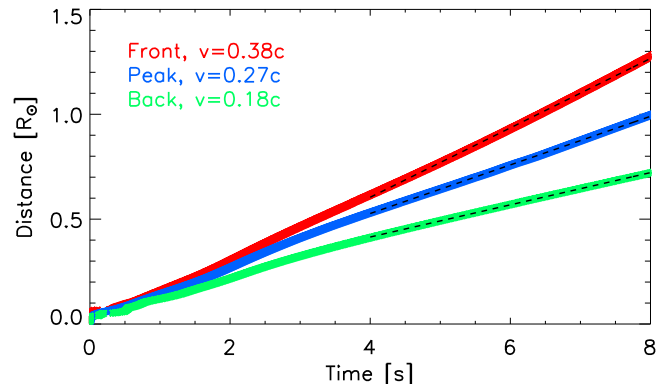


**Figure 4.** Position of the front, peak, and back of the electron beam as a function of time. The dashed lines are linear fits to these positions from 3.5 to 8 s, with the gradient providing a constant velocity, indicated in the plot legend.

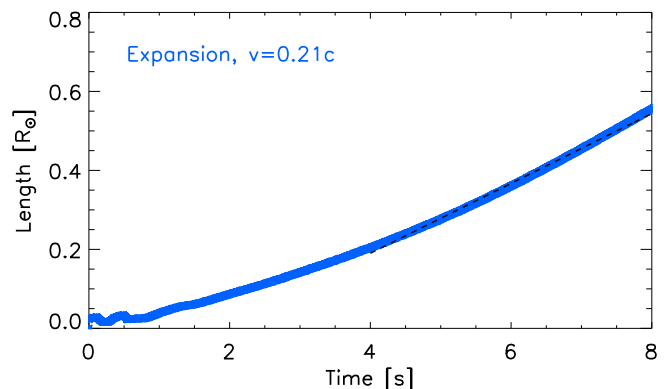


**Figure 5.** Length of the electron beam, found from the distance between the front and back. The dashed line is a linear fit to the length from 4 to 8 s, with the gradient providing a constant velocity for the beam expansion, indicated in the plot legend.

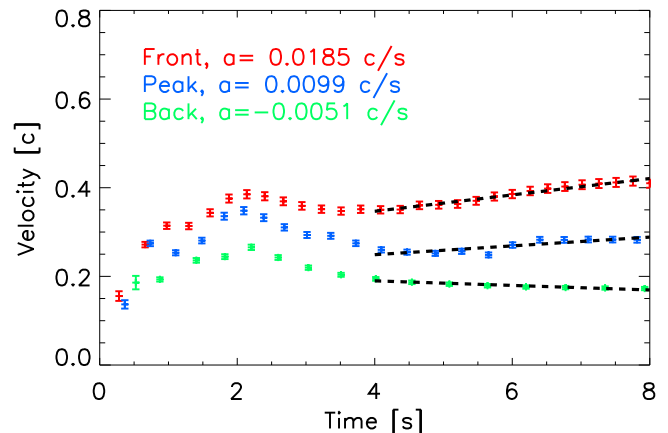


**Figure 6.** Velocity of the front, peak, and back of the electron beam, derived from Figure 4. The dashed line is a linear fit to the velocities from 4 to 8 s, with the gradient providing a constant acceleration, indicated in the plot legend.

$t = 2.1, 3.2, \text{ and } 6.3 \text{ s}$  the positions are  $r = 0.25, 0.39, \text{ and } 0.75 R_\odot$ , respectively.

The motion of electrons and Langmuir waves can be described as a beam-plasma structure using gas-dynamic theory (e.g., Ryutov & Sagdeev 1970; Kontar et al. 1998; Mel'Nik et al. 1999). Electrons are able to fully relax to a plateau in velocity space, then the beam-plasma structure

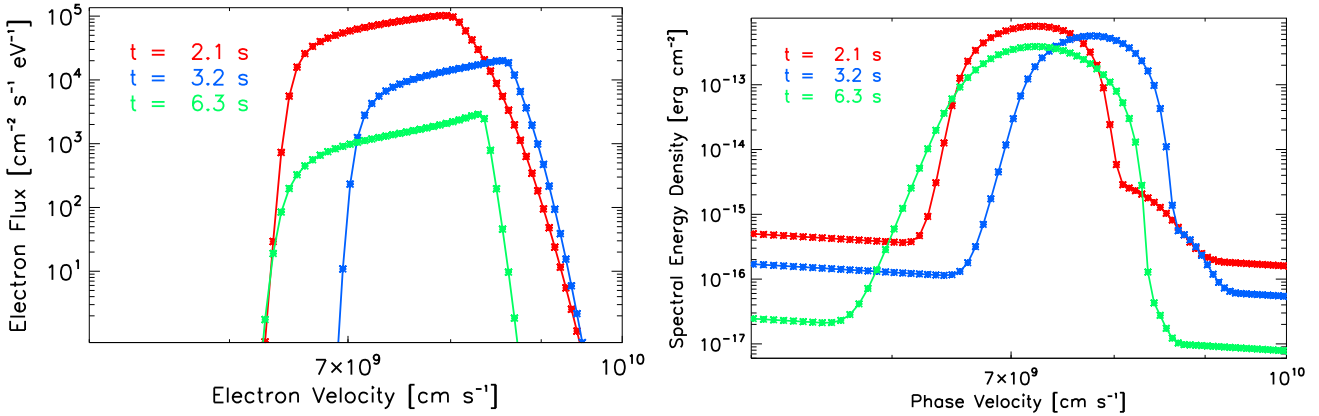


**Figure 7.** Electron flux and Langmuir wave spectral energy density as a function of velocity. The different times show the increase and subsequent decrease in wave-particle resonant velocities.

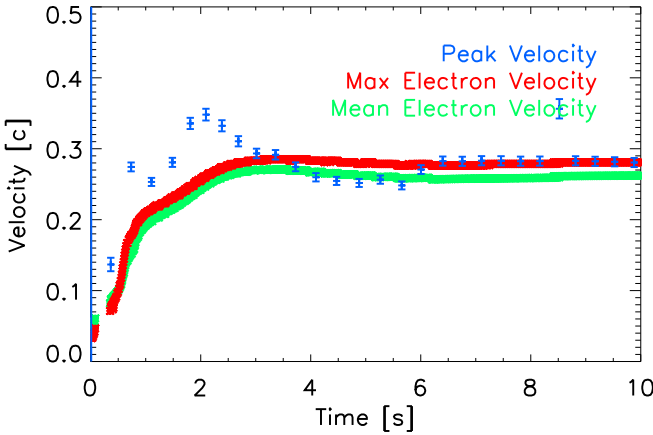


**Figure 8.** Peak velocity of the electron beam from Figure 6 overplotted on the maximum and mean velocities in the electron distribution function as a function of time. The peak velocity appears to track well the maximum electron velocity in the plateau.

moves through space with the mean velocity of the electrons  $v_{bp} = (v_{\max} + v_{\min})/2$ , where  $v_{\max}$  and  $v_{\min}$  are the minimum and maximum velocities within the plateau. If the electrons have not fully relaxed then the mean electron velocity within the beam can be found using

$$\bar{v}(r, t) = \frac{\int_{v_{\min}}^{v_{\max}} f(v, r, t) v dv}{\int_{v_{\min}}^{v_{\max}} f(v, r, t) dv}. \quad (4)$$

We show in Figure 8 both the mean electron velocity and the velocity where the electron distribution  $f(v)$  has a maximum, at the position corresponding to the peak brightness temperature, as a function of time. We also show the velocity derived from the motion of the peak brightness temperature.

At the earliest times, before 3 s, the peak velocity is significantly higher than either the maximum or mean velocity of the electrons that form the plateau. As explained above, this is because the peak velocity is tracking the position of the peak brightness temperature. Indicated in Figure 7, this position increases with time not just because of electron movement through space but also because the related electron beam is at

higher (and then lower) velocities at different points in time. The apparent motion is thus faster than the velocity of the electrons generating the Langmuir waves.

At later times the peak velocity is similar to that of the electrons resonating with the Langmuir waves. There is a tendency to propagate at the same velocity as the maximum velocity of electrons within the plateau at the same spatial location. This is different from what is expected from gas-dynamic theory, which predicts the mean velocity of electrons would track the motion. The anomalous point around 8.5 s is just related to the discretization of the grid in velocity space, and the sharp, localized increase in velocity should be spread over a longer time frame.

#### 4. Electron Beam Parameters

The number density of electrons at specific velocities (the phase-space density) of the injected electron beam has a significant effect in dictating how fast the electron beam will travel through the coronal and interplanetary plasma. Typically, the more high-energy electrons in the beam, the faster it will go. Two key beam parameters that dictate this are the initial spectral index  $\alpha$  and the initial beam density  $n_b$ .

In this section we will explore how the velocity of the front, peak, and back of the electron beam ( $v_f$ ,  $v_p$ ,  $v_b$ , respectively) are affected by  $\alpha$  and  $n_b$ . To estimate how they affect beam propagation we varied the initial spectral index such that  $6 \leq \alpha \leq 10$  and the initial beam density such that  $10^{-1.5} \leq n_b/n_e \leq 10^{-3.5}$ , where  $n_e = 3 \times 10^9 \text{ cm}^{-3}$  at the injection site. The rest of the beam parameters are the same as Section 3 and are given in Table 1.

As shown in Figure 6, the velocity of the electron beam varies as a function of distance. To compare simulations with a single velocity, we find the average velocity over the distance range that corresponds to plasma frequencies 30–70 MHz. These frequencies relate to distances  $3.0 \times 10^{10}$ – $5.3 \times 10^{10}$  cm or  $0.44$ – $0.76 R_\odot$ . We find the average velocity from the gradient of a linear fit to distance as a function of time.

##### 4.1. Electron Beam Velocities

The velocity at the front of the electron beam is shown in Figure 9 for different values of  $\alpha$  and  $n_b$ . The velocity increases as the spectral index decreases and the initial beam density

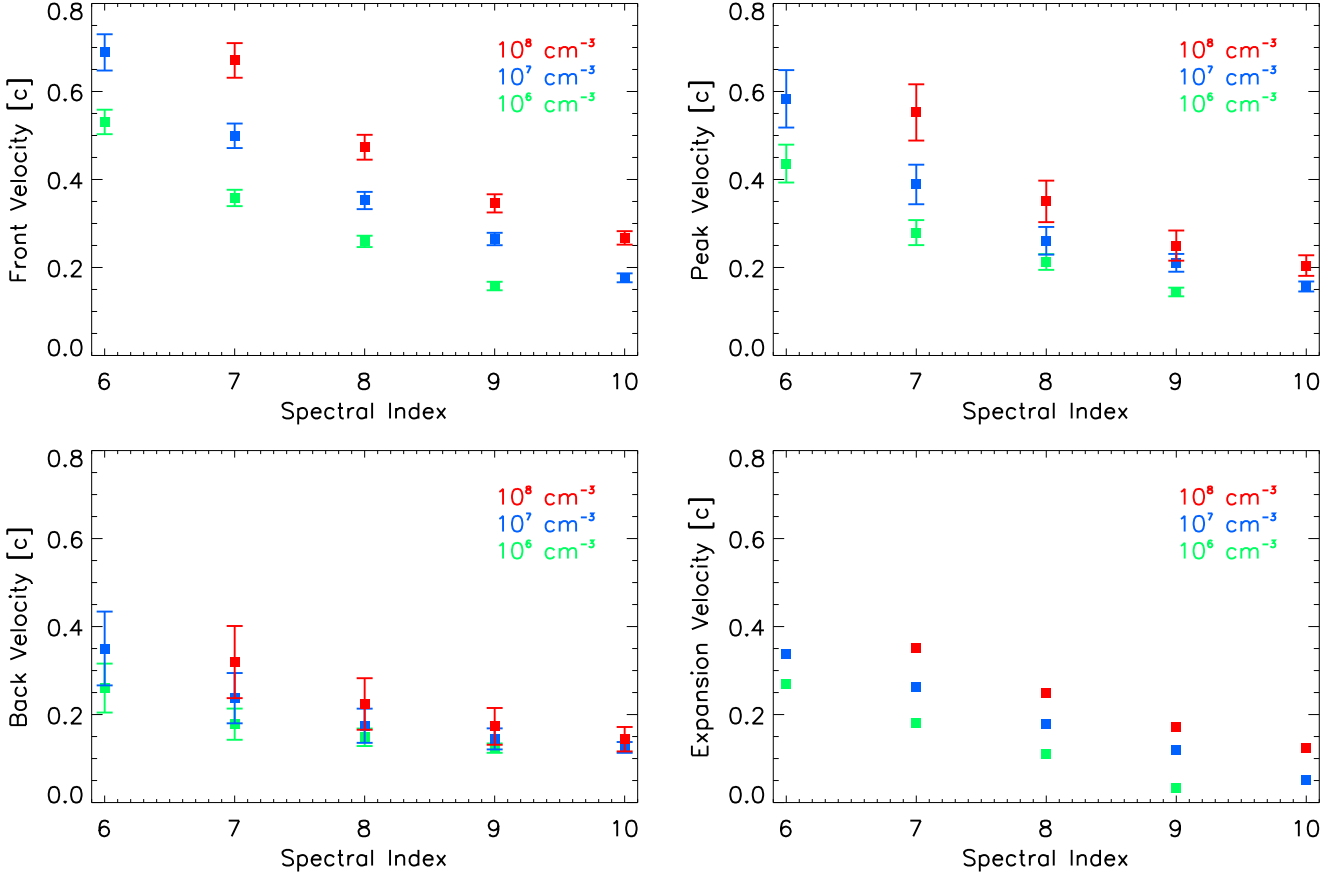


**Figure 9.** Apparent velocity of the front, peak, back, and expansion of the beam as a function of spectral index for beam densities  $10^6$ ,  $10^7$ , and  $10^8 \text{ cm}^{-3}$ . The velocities are found using a linear fit of distance and time between 30 and 70 MHz. The width of the error bars indicates the mean width of the electron distribution function when the front, peak, and back velocities are calculated.

increases. Both parameters show that increasing the number of electrons at velocities higher than the thermal speed controls how fast the front of the electron beam moves. The front velocity,  $v_f$ , when  $n_b = 10^7 \text{ cm}^{-3}$  and  $\alpha = 6$  is slightly lower than we might expect because substantial Langmuir waves are generated by electrons with velocities  $v_{\max} = 0.7c$ , and would likely be generated by higher-velocity electrons, if included in the simulation.

The peak velocity,  $v_p$ , of the electron beam changes as the initial density and spectral index of the electron beam are altered, shown in Figure 9. Similar to  $v_f$ ,  $v_p$  increases for smaller initial spectral indices and larger initial beam densities. The size of the peak velocities are smaller than the front velocities, such that the mean  $\pm$  the standard deviation of  $v_p/v_f$  is  $0.80 \pm 0.06$ .

The velocity of the back of the beam,  $v_b$ , varies in a similar manner, increasing with decreasing initial spectral index and increasing initial beam density, shown in Figure 9. The back velocity is smaller such that  $v_b < v_p < v_f$ . The mean ratio of  $v_b/v_p$  is  $0.67 \pm 0.08$  while the mean ratio of  $v_p/v_f$  is  $0.54 \pm 0.1$ . The variation in the back velocity as the initial beam parameters are changed is much less than the front and peak velocities. The back velocity is heavily dependent on the thermal velocity of the background Maxwellian plasma; we investigate this dependence in the next section.

The mean width of the electron distribution function when the front, peak, and back velocities are calculated are displayed using error bars in Figure 9. The width,  $dv$ , is defined using the

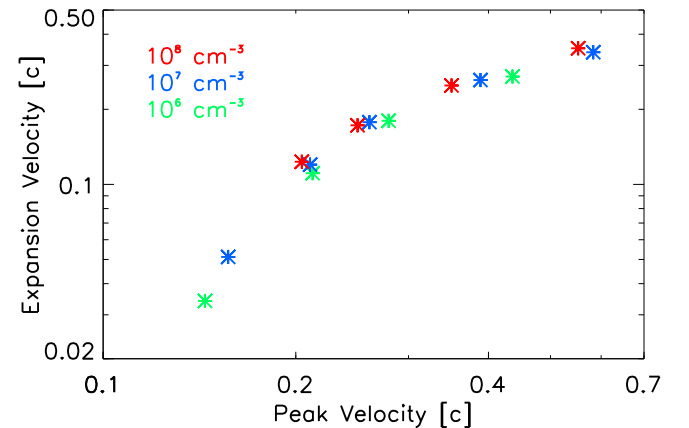


**Figure 10.** Expansion velocity as a function of peak velocity, using the results shown in Figure 9.

full width, 10% maximum on account of the sharp decrease in the distribution function afterward (see Figure 7). Defining  $dv$  using the FWHM reduces the width by 2, or 1.5 for the back velocities. The ratio  $dv/v$  gives an indication of how much quasilinear diffusion the beam has undertaken. Mean ratios for the front, peak, and back of the beam are 10%, 20%, and 40%, respectively. The low value for  $dv/v$  indicates that the beams are only weakly relaxing, in comparison to the full plateau which is assumed using gas-dynamic theory. The mean ratio increases toward the back of the beam on account of the higher

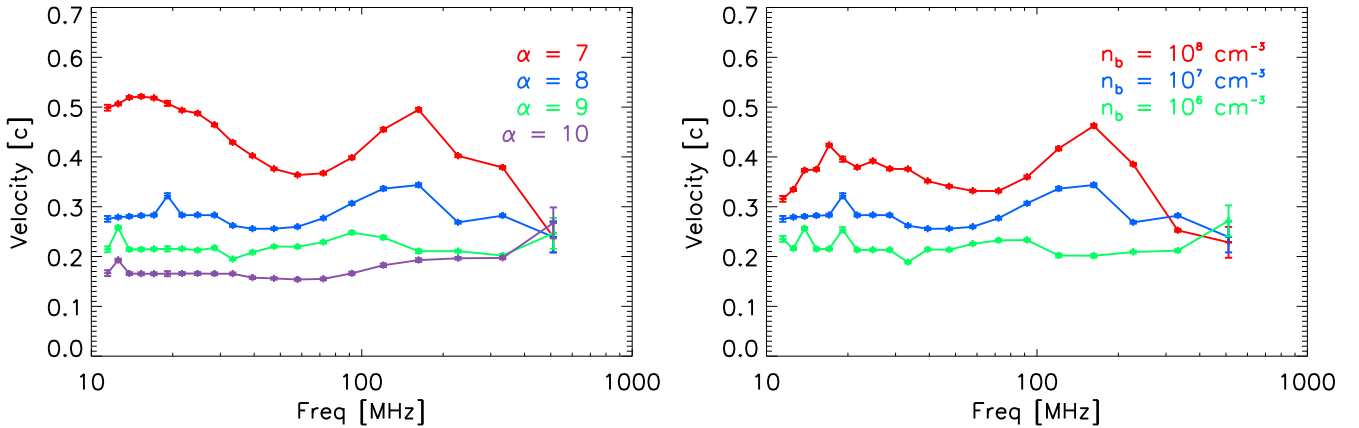


**Figure 11.** Beam velocity as a function of plasma frequency. Left: the initial spectral index  $\alpha$  varies from 7 to 10 with an initial beam density of  $n_b = 10^7 \text{ cm}^{-3}$ . Right: the initial beam density varies from  $n_b = 10^6 \text{ cm}^{-3}$  to  $n_b = 10^8 \text{ cm}^{-3}$  with an initial spectral index of  $\alpha = 8$ .

beam densities at lower velocities, making the quasilinear diffusion quicker and hence more pronounced.

The change in beam length as a function of time, the expansion velocity  $\Delta v \approx v_f - v_b$ , is shown in Figure 9. It is not surprising that we find  $\Delta v$  having similar behavior to  $v_f$  and  $v_b$ , increasing with higher initial beam densities and lower initial spectral indices.

The expansion velocity has a linear correlation with the peak velocity, shown in Figure 10, with a Pearson correlation coefficient of 0.98. As the peak velocity increases, the expansion velocity increases. The latter tends to zero around  $v_{\text{peak}} = 0.1 c$ . Around this velocity, Landau damping from the 1 MK background plasma suppresses any wave generation by the electron beam; this is the reason why  $v_{\text{peak}}$  does not go any lower.

#### 4.2. Beam Velocity Evolution

In the previous section we investigated beam velocities by averaging between 70 and 30 MHz to obtain a single velocity for comparison purposes. However, the beam velocity is not constant with either time or space, as shown in Figure 6. It varies, depending on the minimum and maximum electron velocities that are important for the beam–plasma interaction with Langmuir waves.

We show in Figure 11 the velocity evolution of the peak brightness temperature as a function of frequency for simulations with different initial spectral indices and beam densities. The increase and subsequent decrease in beam velocity at frequencies above 100 MHz is consistent with all simulations, with the explanation given in Section 3.2.

At frequencies below 100 MHz, we observe an increase in the velocity of the peak brightness temperature for some simulations but not others. For the simulations where the number of high-energy electrons (at deca-keV energies) is higher, due to a higher beam density or a lower spectral index, the velocity tends to increase and then decrease. For example, when  $\alpha = 7$  and  $n_b = 10^7 \text{ cm}^{-3}$ , there are enough deca-keV electrons such that increasingly higher electron velocities become relevant to the beam–plasma structure with distance. This occurs until a point where the decrease in beam density from the expanding flux tube starts making wave generation more difficult. Increasingly lower electron velocities then become more relevant and the velocity of the peak brightness temperature decreases. For the simulations where, e.g.,  $\alpha = 10$  and  $n_b = 10^7 \text{ cm}^{-3}$ , this point occurs before 100 MHz and we

do not see a significant change in the velocity. There are some anomalous points in Figure 11 at frequencies below 20 MHz, again related to the discretization of the grid in velocity space, and the sharp, localized increase in velocity should be spread over a wider frequency band.

An increase in the inferred beam velocity from type III bursts has recently been reported by Mann et al. (2018) using LOFAR imaging observations below 100 MHz. They derive velocities from the onset time of the type III burst at different frequencies and find huge increases around 30 MHz, with some bursts reported as superluminal. While the effect we describe above can increase the derived beam velocity from radio bursts, and could play a role in the findings of Mann et al. (2018), it is not likely to explain three-fold increases in velocities, nor provide superluminal velocities. While refraction effects are considered, radio wave scattering at LOFAR frequencies has a more dominant effect (see Kontar et al. 2017), is likely to increase the derived beam speeds, and could explain the apparent beam acceleration.

#### 4.3. Thermal Velocity

The background plasma temperature plays a significant role in governing the largest velocity at which Langmuir waves are damped by the background plasma. Langmuir waves are heavily Landau damped close to the thermal velocity. Our previous simulations used a background temperature of 1 MK, giving a thermal velocity of  $v_{te} = 3.9 \times 10^8 \text{ cm s}^{-1}$  or  $0.013c$ . To show the effect of the background temperature, Figure 12 presents a snapshot of the Langmuir wave spectral energy density for four different simulations using the same initial electron beam parameters ( $\alpha = 6$ ,  $n_b = 10^6 \text{ cm}^{-3}$ ) but with different background temperatures of 1, 2, 4, and 8 MK. This corresponds to  $v_{te} = 0.013$ ,  $0.018$ ,  $0.026$ , and  $0.037c$ , respectively. It is clear from Figure 12 that a higher background temperature increases the minimum velocity where a substantial level of Langmuir waves are generated.

Higher background temperatures increase the velocities of the back of the electron beam, shown in Figure 13. This is because slower electrons are no longer able to generate substantial levels of Langmuir waves in the presence of high Landau damping. For temperatures of 1 MK, the back of the beam relates to Langmuir waves with phase velocities around  $0.25c$ , well above their lowest phase velocities. At temperatures of 8 MK, the back of the beam relates to Langmuir waves with the lowest phase velocities. This behavior is captured by the

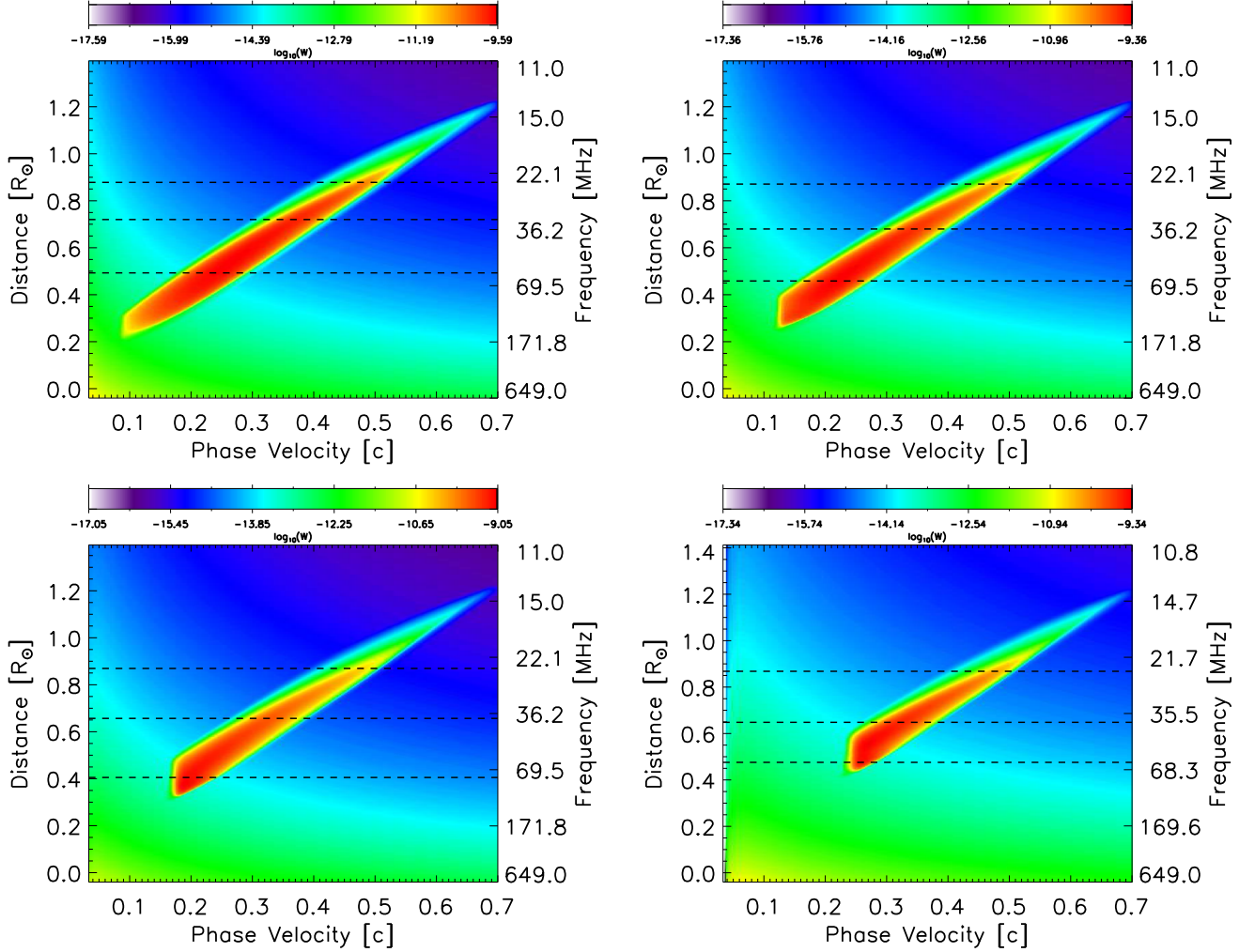


**Figure 12.** Langmuir wave spectral energy density after 4 s of beam propagation. The background temperature varies as 1, 2, 4, and 8 MK from top left to bottom right. The front, peak, and back of the electron beam, found from the resulting radio brightness temperature, are shown by the horizontal dashed lines. Note the decrease in Langmuir waves at lower phase velocities for higher background temperatures.

ratio of  $v_b/v_{te}$  which is 20 for  $T_e = 1$  MK and 9.4 for  $T_e = 8$  MK. Conversely, the front of the beam is not influenced very much by the background temperature as the corresponding

Langmuir waves at high phase velocities are not damped by the background electron distribution.

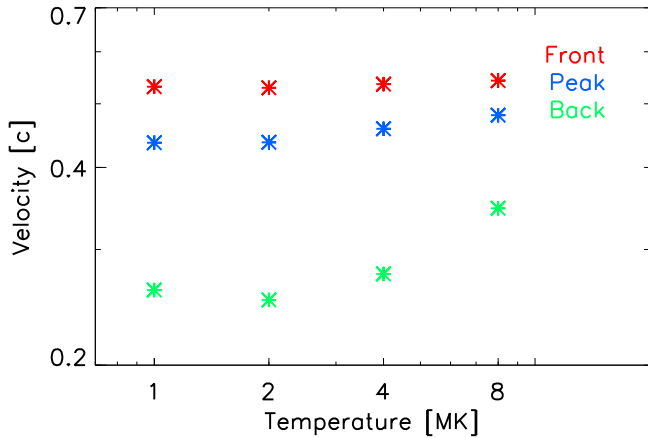


**Figure 13.** Front, peak, and back velocities for an electron beam traveling through background plasma with temperatures of 1, 2, 4, and 8 MK. Velocities are found using a linear fit of distance and time between 20 and 35 MHz, corresponding to 40–70 MHz assuming harmonic emission.

## 5. Type III Bandwidth and Drift Rate

### 5.1. Type III Bandwidth

The instantaneous bandwidth of a type III burst is the width in frequency space at any single point in time. In the context of the electron beam, this relates to the range of plasma frequencies within the beam length, i.e., the difference in plasma frequency between the position of the front and the back of the electron beam.

Figure 14 shows how the bandwidth is different for different initial spectral indices. The frequency associated with each bandwidth is the background plasma frequency at the location of the peak of the electron beam. For all frequencies, the bandwidth is higher for lower initial spectral indices. This is expected from Figure 9 as a lower initial spectral index creates a longer beam. There is also a systematic decrease in the bandwidth as the frequency decreases. This is related to the bulk decrease in magnitude of the background electron density gradient. Over nearly an order of magnitude in frequency the change in bandwidth from the spectral index is reasonably

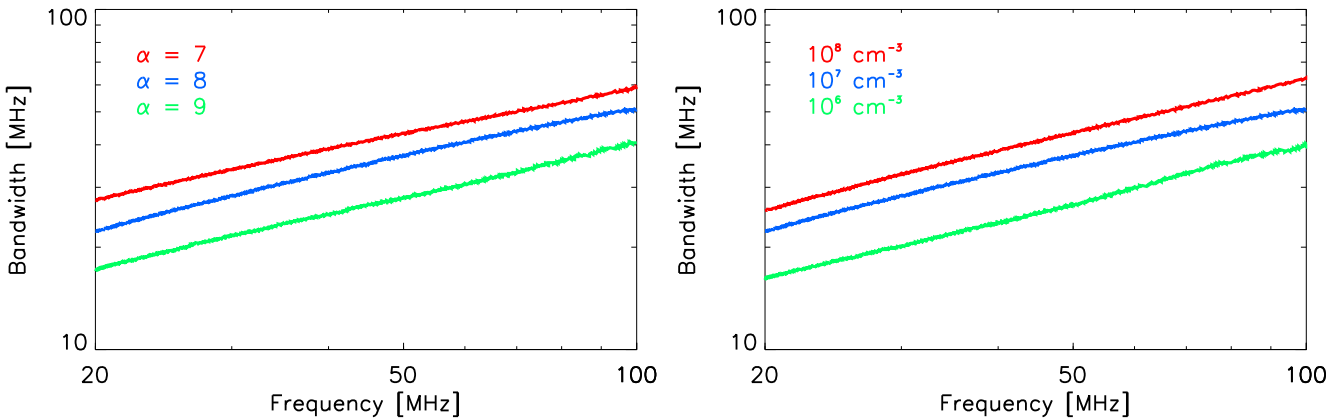


**Figure 14.** Instantaneous bandwidth of the electron beam as a function of the plasma frequency. Left: the initial spectral index  $\alpha$  varies from 7 to 9 with an initial beam density of  $n_b = 10^7 \text{ cm}^{-3}$ . Right: the initial beam density varies from  $n_b = 10^6 \text{ cm}^{-3}$  to  $n_b = 10^8 \text{ cm}^{-3}$  with an initial spectral index of  $\alpha = 8$ .

significant, with the bandwidth at 100 MHz when  $\alpha = 9$  being the same as that at 40 MHz when  $\alpha = 7$ .

The bandwidth is affected by the initial beam density, shown in Figure 14, with a higher initial beam density increasing the bandwidth. Again the change in bandwidth from the initial beam density is significant in comparison to that from the decrease in magnitude of the background electron density gradient at lower frequencies.

### 5.2. Type III Drift Rate

The drift rate of type III bursts can be found using the variation of frequency with time at a given intensity point (e.g., time of peak intensity in each frequency channel), found using the rise, peak, or decay times in the type III dynamic spectra, relating to the motion of the front, peak, or back of the electron beam as a function of time. Figure 15 shows the drift rate inferred from the rise, peak, and decay times of the fundamental emission calculated from the Langmuir wave spectral energy density. The large difference in magnitude between the front and back drift rates is evident, with the front clearly drifting faster than the back, as expected.

The initial parameters also govern the magnitude of the drift rate as a function of frequency. Figure 16 shows how the inferred drift rate changes when the initial spectral index is varied. Similar to the bandwidth, the magnitude of the drift rate decreases as the initial spectral index is increased. Compared to the bandwidth, the initial spectral index is less significant for the drift rate compared to the decrease in drift rate from the reduced background electron density gradient at lower frequencies. For example, the drift rate at 100 MHz when  $\alpha = 9$  is the same as the drift rate at 70 MHz when  $\alpha = 7$ .

The initial beam density also affects the drift rate, with a smaller initial beam density leading to a lower drift rate magnitude, shown in Figure 16. Again, the change in drift rate from the initial beam density is less than that from the bulk decrease in background density density gradient at distances farther from the Sun. For example, the drift rate at 100 MHz when  $n_b = 10^6$  is the same as that at 70 MHz when  $n_b = 10^8$ .

The drift rates around 100 MHz are very similar to those derived from type III radio observations at similar frequencies by Alvarez & Haddock (1973). However, a power-law fit to the peak curve in Figure 15 gives a spectral index of 1.52, lower than the 1.84 found in Alvarez & Haddock. The drift rates are slightly higher than those given by Achong & Barrow (1975), between 26 and 36 MHz, and by Reid & Kontar (2018),

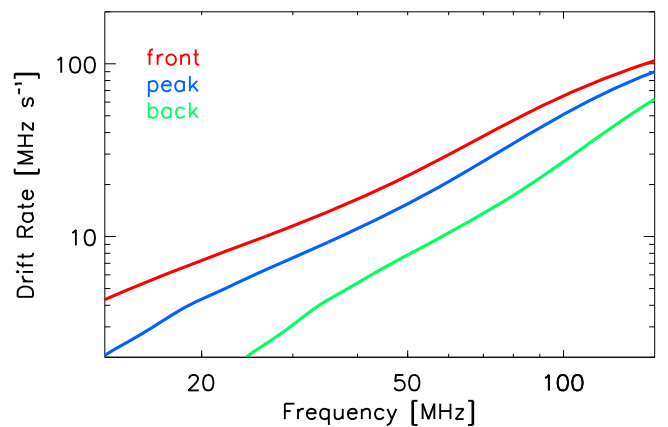


**Figure 15.** Frequency drift rate magnitude of the rise, peak, and decay of the type III burst as a function of frequency. This related to the change in position of the front, peak, and back of the beam as a function of time. The initial beam density is  $n_b = 10^7 \text{ cm}^{-3}$  and the initial spectral index is  $\alpha = 8$ .

between 30 and 70 MHz. The spread in drift rates from the different electron beam parameters is similar to the spread in values presented in both studies. Moreover, the spectral index of 1.52 is closer to those presented in the latter two studies, with a larger spectral index found from the back of the beam matching the results in Reid & Kontar (2018).

Using numerical simulations, a decrease in the magnitude of the drift rate has previously been shown by Li & Cairns (2013) at 120 and 80 MHz for an increasing initial power-law spectral index. Similarly, Kontar (2001b) showed that decreasing the beam density or the characteristic velocity of a Maxwellian electron beam decreases the magnitude of the drift rate. We highlight that the change in drift rate from the initial beam parameters does not significantly alter any type III drift rate as a function of frequency, compared to the effect of the background density model. This is despite a doubling in the inferred peak velocity between spectral indices  $\alpha = 6$  and  $\alpha = 7$ .

## 6. Discussion

We have shown that the initial electron beam parameters play a significant role on the dynamics of the electron beam as it travels through the heliosphere. We initially assumed that the electron beam was a power-law in velocity space with a spectral index  $\alpha$ . This led to the spectral index and the beam

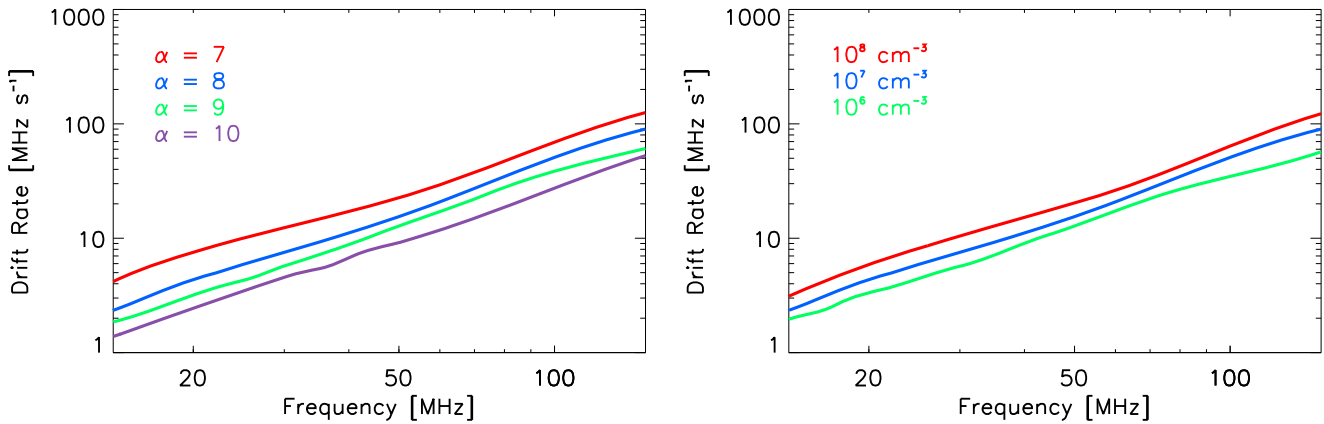


**Figure 16.** Frequency drift rate magnitude of the electron beam as a function of plasma frequency. Left: the initial spectral index  $\alpha$  varies from 7 to 10 with an initial beam density of  $n_b = 10^7 \text{ cm}^{-3}$ . Right: the initial beam density varies from  $n_b = 10^6 \text{ cm}^{-3}$  to  $n_b = 10^8 \text{ cm}^{-3}$  with an initial spectral index of  $\alpha = 8$ .

density playing the dominant role for the phase space density of the electron beam.

### 6.1. Initial Broken Power Law

We can instead assume that the electron beam is injected as a broken power law in velocity space with some break velocity  $v_{\min} \leq v_0 \leq v_{\max}$ . The source function changes from  $S(v, r, t) \propto v^{-\alpha}$  in Equation (1) to

$$S(v, r, t) \propto A_{v2} \begin{cases} 1, & \text{if } v \leq v_0 \\ (v_0/v)^{\alpha}, & \text{if } v > v_0. \end{cases} \quad (5)$$

where

$$A_{v2} = n_b \left[ v_0 - v_{\min} + \frac{v_{\max} (v_{\max}/v_0)^{-\alpha} - v_0}{1 - \alpha} \right]^{-1}. \quad (6)$$

As the distribution below  $v_0$  is flat, the number of electrons at velocities higher than a few  $v_{\min}$  are much greater than in Equation (1) for a given beam density  $n_b$ . The broken power law is necessary to have very high densities contained within electrons above certain energies (e.g., 20 keV). These are required to explain the hard X-ray observations observed in the low solar atmosphere (Holman et al. 2011).

Using the broken power law, we ran simulations with varying initial beam densities to show the effect of changing  $v_0$ , the break velocity. Figure 17 shows how the velocities increase as  $v_0$  is increased. Injecting an electron beam with a high break velocity has a significant effect on the resultant velocities of the electron beam. This is not surprising given that we are significantly increasing the phase space density of the high-energy electrons by increasing  $v_0$ . The simulation with  $v_0 = 0.23 c$  and  $n_b = 10^4 \text{ cm}^{-3}$  generated significant Langmuir waves with phase velocity  $v_{\max}$ . Beam velocities would have been higher if our simulation box extended further than 0.7c.

The effect of changing the break velocity,  $v_0$ , has been investigated by Li & Cairns (2013), who showed that increasing it significantly increases both the peak velocity and the peak flux of fundamental radio wave emission. We show here that  $v_0$  will have a significant effect on the front and back velocities of an electron beam.

The acceleration of a broken power law is perhaps not a physically probable accelerated distribution. There is no simple physical explanation why the accelerated electron distribution

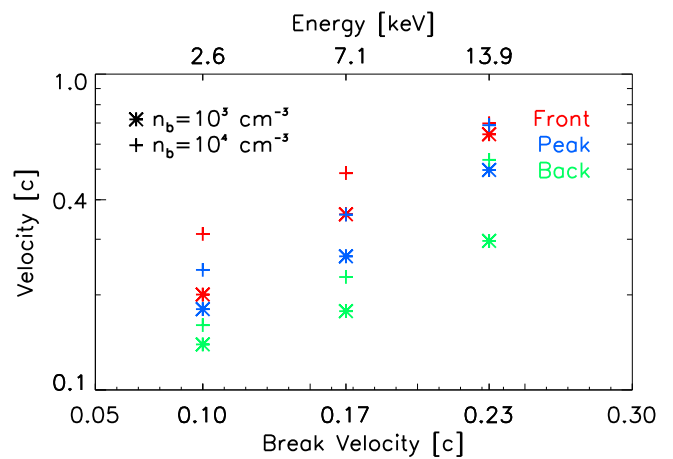


**Figure 17.** Front, peak, and back velocities for an electron beam with an initial broken power-law velocity distribution using different break velocities. Different beam densities of  $10^3$  and  $10^4 \text{ cm}^{-3}$  are shown. Velocities are found using a linear fit of distance and time between 30 and 70 MHz.

would form a plateau below  $v_0$ , unless caused by some other physical process like Langmuir wave generation. A high break velocity could be caused during particle acceleration in the presence of Coulomb collisions from a high-temperature plasma. Electrons below the break velocity could be susceptible to a significant level of collisions with the background plasma within the acceleration timescale. During the latter stages in solar flares, when the coronal plasma reaches temperatures in excess of 10 MK, collisions around the acceleration region will be significantly higher.

### 6.2. Langmuir Wave Spectral Energy Density

We calculated the front, peak, and back of the electron beam from the derived fundamental emission brightness temperature (Equation (3)) assuming a saturation of ion-sound waves. The peak of the brightness temperature is proportional to  $W_{\max}(k, r, t)/k^2$ . The rationale for using the radio brightness temperature is the desire to use type III bursts for remote sensing of electron beam properties.

Instead of using the radio brightness temperature we can instead use the Langmuir wave spectral energy density. For a given time we find the value of  $W_{\max}$  at each position, and then use the corresponding FWHM to find the front, peak, and back of the electron beam. The absence of  $1/k^2$  means that Langmuir

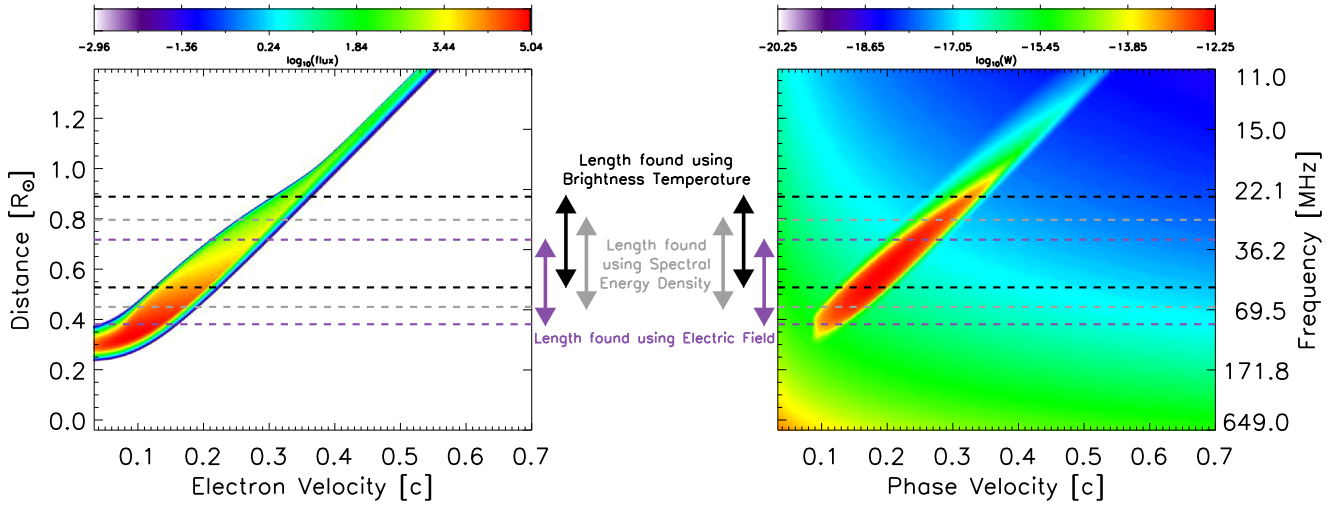


**Figure 18.** Electron flux and Langmuir wave spectral energy density at 6 s for the initial electron beam parameters given in Table 1. The corresponding front and back of the electron beam are indicated by horizontal dashed lines, found from the brightness temperature (black), the peak value of the Langmuir wave spectral energy density (gray), and the Langmuir wave electric field (purple).

waves with higher  $k$ -vectors (lower phase velocities) play a more significant role in determining the front, peak, and back of the beam.

Another metric that can be used is the FWHM of the Langmuir wave electric field to find the front, peak, and back of the electron beam. The Langmuir wave electric field is a measurable quantity in the solar wind, unlike the Langmuir wave spectral energy density. The electric field associated with the Langmuir waves can be found from  $E^2(r, t) = 8\pi U_w(r, t)$ , where  $U_w(r, t)$  is their energy density, found by integrating  $W(k, r, t)$  over  $k$ . The electric field is even more influenced by Langmuir waves with higher  $k$ -vectors than the peak spectral energy density.

We show the comparison between the front and back of the electron beam using the radio brightness temperature, the peak spectral energy density, and the electric field in Figure 18. The simulation is the same as shown in Figure 3 at  $t = 6$  s. The difference between the three metrics is clear, with the method using radio brightness temperature being coincident with Langmuir waves at higher phase velocities and the method using the electric field being coincident with Langmuir waves at lower phase velocities. The length of the electron beam using all three metrics remains similar, around  $0.35 R_\odot$  at  $t = 6$  s. The velocities attributed to the front and back of the electron beam are higher when the brightness temperature is used and lower when the electric field is used.

### 6.3. Beam Energy Density and Brightness Temperature

The complicated plasma emission mechanism has hampered the use of radio bursts as a diagnostic for electron beam energetics. For the first time we present an estimate for the energy density contained within the electrons that produce the type III emission as a function of peak radio brightness temperature of a type III burst at different frequencies. The electron energy density can be found from the electron distribution function  $f(v, r, t)$  using

$$U_{\text{beam}}(r, t) = 0.5m_e \int_{v_{\min}}^{v_{\max}} f(v, r, t)v^2 dv. \quad (7)$$

For a given frequency, the peak energy density correlates to the peak brightness temperature, shown in Figure 19 using all

simulations presented in Section 4, which have different initial electron beam densities and velocity spectral indices. At a single frequency, the greater the energy density of the electrons producing the Langmuir waves, the higher the radio brightness temperature they generate. The energy density can be fit with a power law at different frequencies, with the fit parameters given in Table 2. The spectral index at each frequency is approximately 0.5 but the amplitude decreases with decreasing frequency,  $f$ , and has the approximate relationship of  $10^{-38.4}f^3$  for  $f$  in Hz. We can then approximate the energy density of the electrons responsible for the radio brightness temperature  $T_T$  using

$$U_{\text{beam}}(f, t) = 10^{-38.4}f^3 T_T^{0.5}. \quad (8)$$

The correlation between beam energy density and brightness temperature can be explained using the analytical gas-dynamic solutions. From Mel'nik et al. (2000) and Kontar et al. (2001) we expect the peak Langmuir wave energy density to be

$$W^{\max}(v) \propto m_e n_b v^3. \quad (9)$$

We can substitute this into the beam brightness temperature, defined in Equation (3), obtaining

$$T_T^{\max}(r, t) \propto m_e n_b v^5. \quad (10)$$

The relation in Equation (10) provides a close fit to the brightness temperature but an even closer fit is found using the beam energy density

$$T_T^{\max}(r, t) \propto U_{\text{beam}} v^3. \quad (11)$$

The relation is shown in Figure 19 using a constant of proportionality,  $A$ . It deviates slightly for the simulations with lower brightness temperatures. The peak brightness temperature is thus heavily dependent upon the velocity (or energy) of the electrons that are generating the Langmuir waves; electron beams with higher velocities will typically have higher peak brightness temperatures.

Using the beam energy densities we can calculate the total energy of the electrons that are producing the type III emission,  $E_{\text{beam}} = U_{\text{beam}} V$ , by estimating the volume,  $V$ , of the beam. For a

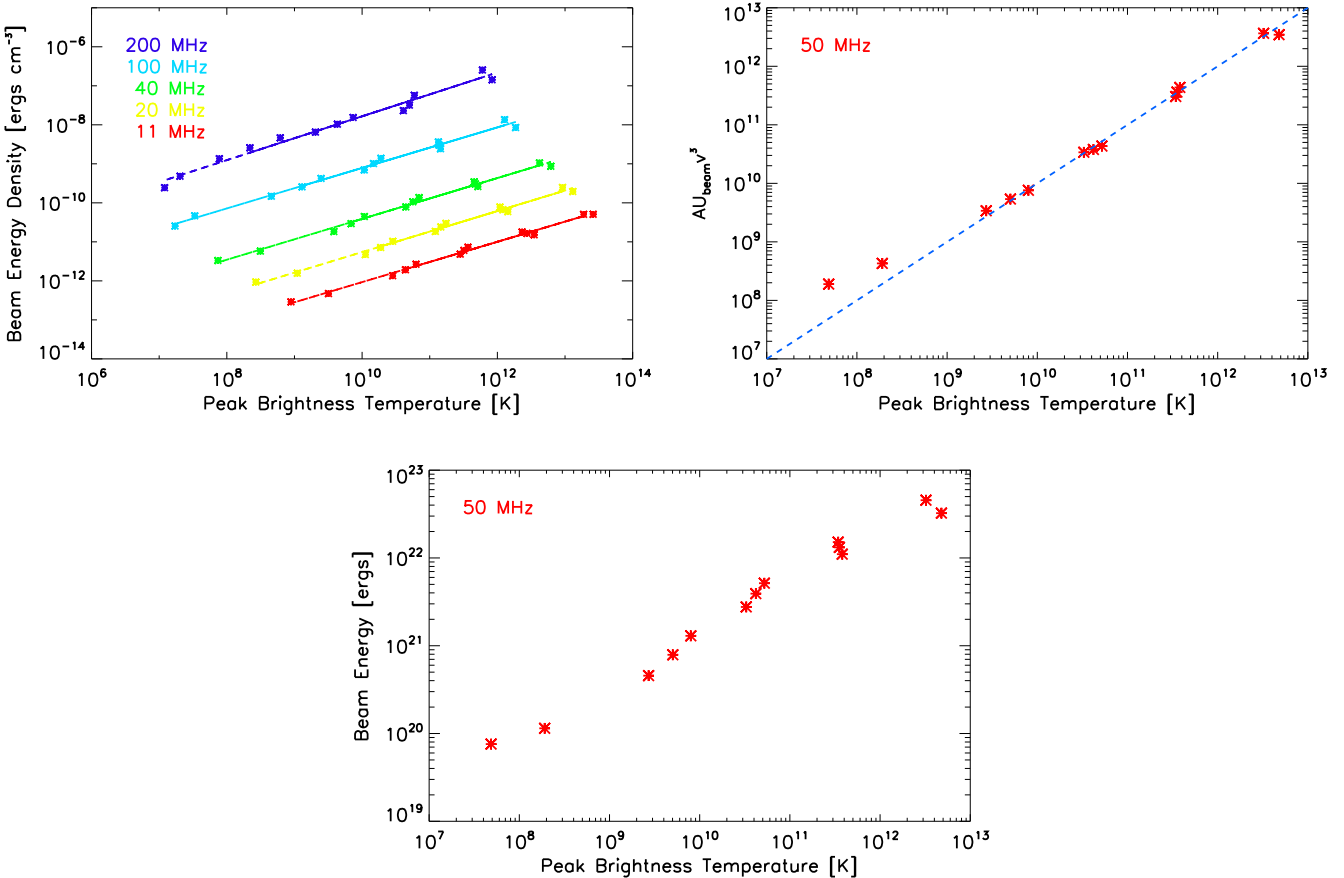


**Figure 19.** Top left: peak beam energy densities as a function of peak brightness temperature for an initial electron beam with an instantaneous time injection. Different points for a single frequency relate to beams with different initial beam densities and spectral indices. Colors represent different frequencies. Top right: analytical estimates of the brightness temperature from gas-dynamic theory using the peak beam energy density  $U_b$ , the beam velocity at the peak brightness temperature and a constant of proportionality,  $A$ . Bottom: beam energy estimated from the energy densities at 50 MHz assuming a source size of 3.2 arcmin. Note that comparisons of energy density and energy with observations can only be done for type IIIs with similar characteristics to our simulations.

**Table 2**  
Fit Parameters Used for Beam Energy Density vs. Peak Brightness Temperature (Figure 19)

Frequency	log Amplitude	Spectral Index
200	-13.4	0.56
100	-14.3	0.52
40	-15.6	0.52
20	-16.5	0.52
11	-17.2	0.52

given frequency, we can estimate the length of the beam in the direction of propagation using a sum of the duration, found from the FWHM of the brightness temperature, and the mean velocity of the electron beam, found from  $\bar{v} = (v_{\text{front}} + v_{\text{back}})/2$ . We estimate the area of the beam using the cross-section of the magnetic flux tube that we use to model the  $r^{-2}$  expansion of the electron beam traveling through the solar corona. We assume an acceleration region cross-section of radius  $d = 10 \text{ Mm}$  which is at a distance of 30 Mm along the cone of expansion. The cross-section at 50 MHz, occurring at 413 Mm along the cone of expansion gives a radius of  $10/30 \times 413 = 138 \text{ Mm}$  (3.2 arcmin). This is quite small compared to observed source sizes (e.g., Kontar et al. 2017). Faster expansion of the magnetic flux tube would increase source sizes but would reduce the energy densities within the beam at a given frequency.

Assuming a Gaussian-distributed source we plot the energies obtained in Figure 19 as a function of peak brightness temperature. As the energy contained in the deca-keV electrons increases, the corresponding radio brightness temperature increases. The energies obtained are quite small in comparison to those measured at 1 au (Krucker et al. 2007; James et al. 2017). However the durations of our electrons beams are significantly lower than those estimated at 1 au, with the number of electrons per second of our largest simulations being comparable to that of James et al. (2017) at 74 keV.

The flux,  $S$ , of our simulated radio bursts can be estimated using the source size  $\theta$  of 3.2 arcmin at 50 MHz. Using the Rayleigh–Jeans law

$$\left(\frac{T_b}{K}\right) = 3770 \left(\frac{S}{\text{SFU}}\right) \left(\frac{\theta}{\text{arcmin}}\right)^{-2} \left(\frac{c}{\text{cm s}^{-1}}\right)^2 \left(\frac{f}{\text{Hz}}\right)^{-2}, \quad (12)$$

we find fluxes of 750 SFU for a brightness temperature of  $10^{11} \text{ K}$ . However, this does not take into account any propagation effects like the scattering of light (e.g., Arzner & Magun 1999; Kontar et al. 2017) that will occur from source to observer.

We can construct an equation for the energy contained in the electrons responsible for the type III emission, based upon observable quantities. The energy density of the beam can be found by combining Equations (12) and (8). As described above, the volume of the beam can be found from the product

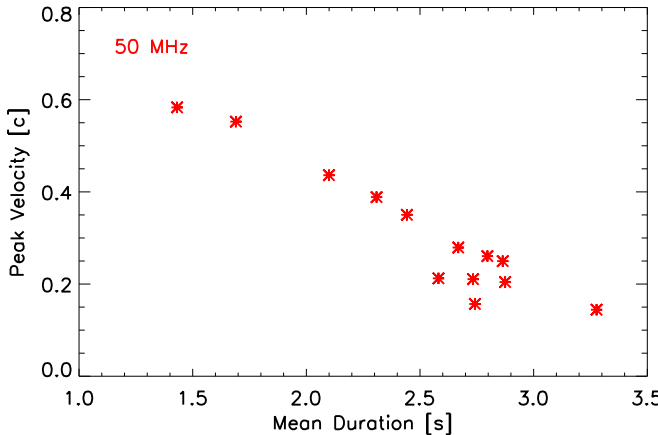


**Figure 20.** Left: mean type III duration as a function of velocity found from the motion of the peak brightness temperature. Both variables were found between 30 and 70 MHz. A strong correlation exists, in line with observational results (Reid & Kontar 2018). Right: range of duration as a function of frequency from the numerical simulations in the range 13–100 MHz. Type III durations from Reid & Kontar (2018) using LOFAR are overplotted, with the blue dashed lines showing the observed standard deviations.

of the length of the beam,  $\bar{v}t_{\text{dur}}$  and the source size,  $\theta^2$ . Again, assuming that the intensity is Gaussian-distributed, one arrives at the following equation:

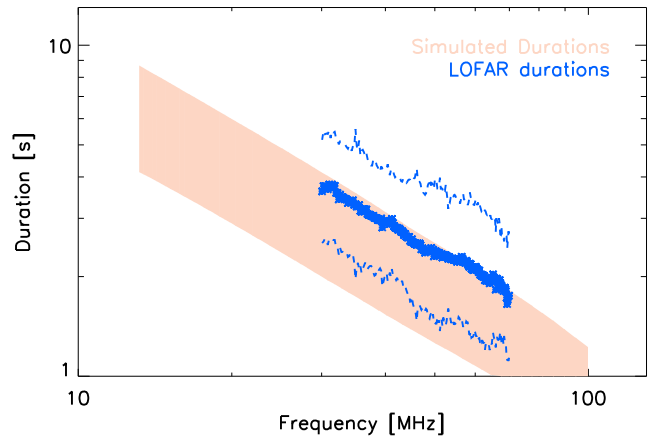
$$\left(\frac{E_{\text{beam}}}{\text{erg}}\right) = 8.8 \times 10^{-7} \left(\frac{\bar{v}}{\text{cm s}^{-1}}\right) \left(\frac{t_{\text{dur}}}{\text{s}}\right) \times \left(\frac{\theta}{\text{arcmin}}\right) \left(\frac{f}{\text{Hz}}\right)^2 \left(\frac{S}{\text{SFU}}\right)^0 \quad (13)$$

where  $E_{\text{beam}}$  is the energy in the electrons responsible for the type III emission. If applied to data, the above equation should only be used for small type III bursts that are similar to our simulations; type III bursts with very long durations of tens to hundreds of seconds at 50 MHz are likely caused by long-duration injection profiles or multiple electron beams, which may change how the radio brightness temperature relates to beam energy density.

Our estimations serve as a first indication of the energy contained within an electron beam using type III bursts, where none currently exists. However, one must be careful as our simulations do not take into account all of the physical processes that will affect the electrons during their propagation. The beam energy estimates do not account for the turbulent background electron density (e.g., Melrose et al. 1986; Kontar 2001b; Reid & Kontar 2010, 2017; Li et al. 2012), which affects the level of Langmuir waves induced by an electron beam. The simulations do not take into account the scattering of light from source to observer, which can smear out the radio light curves in time (e.g., Arzner & Magun 1999; Kontar et al. 2017). They do not model the pitch-angle scattering of electrons from magnetic fluctuations.

#### 6.4. Beam Duration

In a recent study, (Reid & Kontar 2018), we analyzed 31 type III bursts using LOFAR and quantified, among other variables, the FWHM duration of type III burst lightcurves. We found a strong correlation between the type III durations and the velocity of the excitors, derived assuming a density model and second harmonic emission. We find the same correlation between the exciter velocities and the type III durations using the simulated type III brightness temperatures, shown in Figure 20. The velocities found in Reid & Kontar (2018) from the radio bursts are lower than the peak velocities from most of



our simulations, and we are finding the fundamental radio brightness temperature, but the correlation is still strong. Our explanation in Reid & Kontar (2018) holds, that the faster electrons, responsible for the faster derived velocities, have a shorter travel time through one point in space, and hence produce type III bursts with shorter durations.

The type III durations as a function of frequency were also shown in Reid & Kontar (2018). For comparison we plot the range of durations found from the simulations as a function of frequency and overplot the type III durations observed using LOFAR. There is a very good agreement. The observed durations are at the higher end of the simulated ones, expected because the peak velocities estimated from the observations were at the lower end of those found from the simulations. The rise and decay times were also similar between the simulations and the observations, with the simulated rise times being smaller than the decay times.

## 7. Summary

We have simulated the propagation of electron beams through the solar corona, taking into account the resonant interaction with Langmuir waves in the background plasma. We investigated how the front, peak, and back of the electron beam evolve in time, as deduced from the peak type III brightness temperature. We also showed how the electron beam energy density varies with the brightness temperature of fundamental radio emission.

After injection of a power-law distribution in velocity, electrons initially propagate without generation of Langmuir waves. After a distance  $x \simeq \delta d$ , the first waves are generated. The velocity initially increases with distance as higher-energy electrons produce significant Langmuir wave spectral energy density. As the injected distribution is a power law, the maximum velocity increases as higher-velocity electrons start to generate Langmuir waves. Later the velocity of the type III source decreases as a function of distance from the Sun. The FWHM length of the source generating a type III burst increases as a function of time, with the rate of expansion (expansion velocity) being the difference between the front and back velocities. The faster beams expand more rapidly and the front of the electron beam moves faster than the peak, which in turn moves faster than the back of the beam.

The initial electron distribution affects the type III properties; the velocities of type III bursts will be higher for higher initial electron beam densities and lower initial spectral indices (harder spectrum). Both parameters increase the energy density contained within the electrons that produce radio emission. The higher the energy density in the beam, the more energy that is put into Langmuir waves and consequently the higher the derived brightness temperature.

Energetic electrons are also affected by the magnetic fluctuations that lead to the pitch-angle scattering of the electrons. This plays a role for the higher-energy electrons that we are discounting when characterizing the electron beams. There will also be some effect on the deca-keV electrons and its role on the electron transport has to be investigated.

One of the important processes that affect the comparison of type III bursts and the electron simulation is radio-wave propagation. Since the plasma emission originates at frequencies close to the plasma frequency, the radio waves will be strongly affected by scattering and refraction (e.g., Steinberg et al. 1971; Riddle 1972; Arzner & Magun 1999). Recent observations (Kontar et al. 2017) suggest that the spatial, and hence temporal, characteristics of type III bursts at fundamental frequencies are influenced by radio-wave propagation effects. Specifically, the rise, decay, and duration become dependent on the scattering of radio waves on the way from the radio source to the observer. Therefore, the observed properties of type III bursts will be a convolution of electron transport studied here and radio-wave transport.

With the impending launches of *Parker Solar Probe* and *Solar Orbiter* we will be able to measure in situ the electron beams close to the Sun as they produce radio emission. While they will not observe in situ at frequencies above 10 MHz, the combined observations of energetic electrons, Langmuir waves, and Type III bursts should be able to test the velocities at different parts of the electron beam, and estimate the beam length. A great many more electron beams are likely to be observed close to the Sun than at 1 au, in particular with accompanying Langmuir waves, as beam densities will not have decreased as much in the expanding solar wind plasma. Related to this fact, we predict that higher-energy electrons ( $>10$  keV) will be measured co-temporal with Langmuir waves closer to the Sun, especially at the front of the electron beam. Moreover, the beams that produce type III radio emission are likely to have higher fluxes than those where radio emission is absent, for a given energy. Finally, *Solar Orbiter* should detect the transport change in the beam spectral index by combining X-ray measurements with in situ data.

We acknowledge support from the STFC consolidated grant ST/P000533/1. This work benefited from the Royal Society grant RG130642. H.R. acknowledges Paulo Simoes for useful discussions on the presentation of the results.

## ORCID iDs

Hamish A. S. Reid  <https://orcid.org/0000-0002-6287-3494>  
Eduard P. Kontar  <https://orcid.org/0000-0002-8078-0902>

## References

Achong, A., & Barrow, C. H. 1975, *SoPh*, **45**, 467  
 Alvarez, H., & Haddock, F. T. 1973, *SoPh*, **29**, 197  
 Arzner, K., & Magun, A. 1999, *A&A*, **351**, 1165  
 Dulk, G. A., Goldman, M. V., Steinberg, J. L., & Hoang, S. 1987, *A&A*, **173**, 366  
 Dulk, G. A., Leblanc, Y., Robinson, P. A., Bougeret, J.-L., & Lin, R. P. 1998, *JGR*, **103**, 17223  
 Fainberg, J., Evans, L. G., & Stone, R. G. 1972, *Sci*, **178**, 743  
 Ginzburg, V. L., & Zhelezniakov, V. V. 1958, *SvA*, **2**, 653  
 Gurnett, D. A., & Anderson, R. R. 1976, *Sci*, **194**, 1159  
 Gurnett, D. A., & Frank, L. A. 1975, *SoPh*, **45**, 477  
 Holman, G. D., Aschwanden, M. J., Aurass, H., et al. 2011, *SSRv*, **159**, 107  
 Hughes, M. P., & Harkness, R. L. 1963, *ApJ*, **138**, 239  
 James, T., Subramanian, P., & Kontar, E. P. 2017, *MNRAS*, **471**, 89  
 Klassen, A., Karlicky, M., & Mann, G. 2003, *A&A*, **410**, 307  
 Kontar, E. P. 2001a, *CoPhC*, **138**, 222  
 Kontar, E. P. 2001b, *SoPh*, **202**, 131  
 Kontar, E. P. 2001c, *A&A*, **375**, 629  
 Kontar, E. P., Lapshin, V. I., & Mel'Nik, V. N. 1998, *PIPhR*, **24**, 772  
 Kontar, E. P., & Mel'Nik, V. N. 2003, *PhPl*, **10**, 2732  
 Kontar, E. P., Mel'Nik, V. N., & Lapshin, V. I. 2001, *RaSc*, **36**, 1757  
 Kontar, E. P., Yu, S., Kuznetsov, A. A., et al. 2017, *NatCo*, **8**, 1515  
 Krucker, S., Kontar, E. P., Christe, S., & Lin, R. P. 2007, *ApJL*, **663**, L109  
 Krupar, V., Kontar, E. P., Soucek, J., et al. 2015, *A&A*, **580**, A137  
 Li, B., & Cairns, I. H. 2013, *JGRA*, **118**, 4748  
 Li, B., & Cairns, I. H. 2014, *SoPh*, **289**, 951  
 Li, B., Cairns, I. H., & Robinson, P. A. 2012, *SoPh*, **279**, 173  
 Lin, R. P., Potter, D. W., Gurnett, D. A., & Scarf, F. L. 1981, *ApJ*, **251**, 364  
 Lyubchyk, O., Kontar, E. P., Voitenko, Y. M., Bian, N. H., & Melrose, D. B. 2017, *SoPh*, **292**, 117  
 Magelssen, G. R., & Smith, D. F. 1977, *SoPh*, **55**, 211  
 Mann, G., Breitling, F., Vocks, C., et al. 2018, *A&A*, **611**, A57  
 Mann, G., Jansen, F., MacDowall, R. J., Kaiser, M. L., & Stone, R. G. 1999, *A&A*, **348**, 614  
 Mel'Nik, V. N. 1995, *PIPhR*, **21**, 89  
 Mel'Nik, V. N., Konovalenko, A. A., Rucker, H. O., et al. 2011, *SoPh*, **269**, 335  
 Mel'Nik, V. N., & Kontar, E. P. 1998, *PhyS*, **58**, 510  
 Mel'nik, V. N., Kontar, E. P., & Lapshin, V. I. 2000, *SoPh*, **196**, 199  
 Mel'Nik, V. N., Lapshin, V., & Kontar, E. 1999, *SoPh*, **184**, 353  
 Melrose, D. B. 1980, *Plasma Astrophysics, Nonthermal Processes in Diffuse Magnetized Plasmas*, Vol. 1, 2 (London: Gordon and Breach)  
 Melrose, D. B., Cairns, I. H., & Dulk, G. A. 1986, *A&A*, **163**, 229  
 Parker, E. N. 1958, *ApJ*, **128**, 664  
 Poquerusse, M. 1994, *A&A*, **286**, 611  
 Ratcliffe, H., Bian, N. H., & Kontar, E. P. 2012, *ApJ*, **761**, 176  
 Ratcliffe, H., Kontar, E. P., & Reid, H. A. S. 2014, *A&A*, **572**, A111  
 Reid, H. A. S., & Kontar, E. P. 2010, *ApJ*, **721**, 864  
 Reid, H. A. S., & Kontar, E. P. 2013, *SoPh*, **285**, 217  
 Reid, H. A. S., & Kontar, E. P. 2017, *A&A*, **598**, A44  
 Reid, H. A. S., & Kontar, E. P. 2018, *A&A*, **614**, A69  
 Reid, H. A. S., & Ratcliffe, H. 2014, *RAA*, **14**, 773  
 Reid, H. A. S., & Vilmer, N. 2017, *A&A*, **597**, A77  
 Reid, H. A. S., & Vilmer, N. 2014, *A&A*, **567**, A85  
 Reiner, M. J., & MacDowall, R. J. 2015, *SoPh*, **290**, 2975  
 Riddle, A. C. 1972, *PASAu*, **2**, 98  
 Ryutov, D. D., & Sagdeev, R. Z. 1970, *JETP*, **31**, 396  
 Steinberg, J. L., Aubier-Giraud, M., Leblanc, Y., & Boischot, A. 1971, *A&A*, **10**, 362  
 Suzuki, S., & Dulk, G. A. 1985, *Bursts of Type III and Type V* (Cambridge: Cambridge Univ. Press), 289  
 Takakura, T., & Shibahashi, H. 1976, *SoPh*, **46**, 323  
 Tsytovich, V. N., & ter Haar, D. 1995, *Lectures on Non-linear Plasma Kinetics* (Berlin: Springer), 36  
 Vedenov, A. A. 1963, *JNuE*, **5**, 169  
 Wild, J. P., Sheridan, K. V., & Neylan, A. A. 1959, *AuJPh*, **12**, 369  
 Zaitsev, V. V., Mityakov, N. A., & Rapoport, V. O. 1972, *SoPh*, **24**, 444